Research Article | Vol. 26, No. 25 | 10 Dec 2018 | OPTICS EXPRESS 33428
Optics EXPRESS

Mid-infrared Fourier-domain optical coherence tomography with a pyroelectric linear array

IVAN ZORIN,[1,*] RONG SU,[2] ANDRII PRYLEPA,[1] JAKOB KILGUS,[1] MARKUS BRANDSTETTER[1] AND BETTINA HEISE[1]

[1]*Research Center for Materials Characterization and Non-Destructive Testing, Science Park 2, Altenberger Str.69, 4040 Linz, Austria*
[2]*Manufacturing Metrology Team, Faculty of Engineering, University of Nottingham, Nottingham NG8 1BB, UK*
[*]*ivan.zorin@recendt.at*

Abstract: Optical technology in the mid-infrared wavelength range is currently a rapidly developing field initiated by the availability of novel high-power and spatially coherent sources. Non-destructive testing techniques based on these sources are very promising for industrial and medical applications. However, there are still many engineering problems due to the technical challenges and high prices of the optical elements suitable for the mid-infrared region. In this paper, we report the development and performances of the first mid-infrared Fourier-domain optical coherence tomography based on a supercontinuum source and low-cost pyroelectric detector. The system is designed to operate in the spectral region around 4 μm. Experimental results are demonstrated for detections of embedded microstructures in ceramic materials and subsurface oil paint layers.

1. Introduction

The growing development of high-power, low-noise, mid-infrared (MIR) supercontinuum sources raised a great interest for optical imaging and characterization techniques in medical diagnosis or non-destructive testing (NDT) for engineering materials, such as optical coherence tomography (OCT) and spectroscopy [1]. OCT has shown its feasibility for an emerging number of applications in the field of NDT [2, 3], but multiple scattering is a fundamental limit restricting the imaging depth of OCT systems for investigation of turbid materials. Spatial light modulation methods are a promising technique to overcome this barrier in OCT [4, 5], however, these methods require an extensive control, sophisticated post-processing and numerical optimization [6]. In contrast, the predicted capability of OCT at longer wavelengths [7] promises an improved penetration depth into materials owing to reduced scattering, such that the accuracy of measurement of embedded structures and detection of subsurface defects can be enhanced. If the prediction was correct, OCT, that operates in the MIR range, would open new opportunities for NDT of materials which are opaque or highly scattering in the near-infrared (NIR) and visible (VIS) ranges.

The original time-domain OCT (TD-OCT) [8] with a semiconductor point detector and an axially-scanning reference mirror, performing a cross-correlation between reference and sample fields, is a well-established technique. Such systems operating in the MIR range were shown in [9, 10] and a system applying the wavelength conversion technique is shown in [11]. Nevertheless, TD-OCT is inferior to Fourier-domain OCT (FD-OCT) in the speed and also in the sensitivity, where a fundamental difference of about 20 dB has been demonstrated in [12–14].

FD-OCT in a wavelength range of up to 2 μm has been reported in [15]. It has shown a superior performance for investigation of paintings. To the best of our knowledge, FD-OCT in the MIR range beyond 3 μm has not yet been demonstrated and remains an in-demand challenge. This technical gap has appeared, because the price of the supercontinuum sources is decreasing, while the costs of cameras operating in this wavelength range remains high. Commercially available semiconductor (HgCdTe and InSb) based arrays have much lower specifications in the MIR than

#347409 https://doi.org/10.1364/OE.26.033428
Journal © 2018 Received 4 Oct 2018; revised 16 Nov 2018; accepted 17 Nov 2018; published 7 Dec 2018

Optics EXPRESS

those in NIR and VIS ranges. Usually, they are developed for thermal imaging and infrared analysis and have limited optical designs and dynamic range, while a small band gap [16] makes these cameras noisy and dependent on sophisticated cooling systems.

The high power offered by MIR supercontinuum sources and a current technology state enable application of other types of detectors traditionally used in thermal sensors (e.g. bolometer and pyroelectric focal plane arrays) [16]. Currently, up-conversion modules are becoming a promising tool but such systems are still under development and are costly, technically complex and drawbacks include the low spectral resolution and the nonlinearity of conversion at the wavelengths of interest [17–20]. In this contribution, we demonstrate the first MIR FD-OCT applying a low-cost pyroelectric detector and a supercontinuum source.

2. Mid-infrared OCT system with pyroelectric linear array

2.1. Supercontinuum light source

The low-noise MIR supercontinuum source (NKT Photonics), which is used in the MIR FD-OCT system, emits in the wavelength range from 1.1 µm to 4.4 µm with a sub-nanosecond pulse width and at a repetition rate of 2.5 MHz (adjustable), this is high enough so that during the exposure time, spectral fluctuations are averaged out. Figure 1 depicts the MIR part of the spectrum measured by a Fourier-transform infrared (FTIR) spectrometer (spectral resolution about 2.5 nm).

The outgoing beam of the source with the average power of about 475 mW is efficiently collimated by a parabolic mirror so that a fundamental Gaussian mode with an M^2 quality factor of 1.1 and a beam waist diameter around 3 mm is delivered.

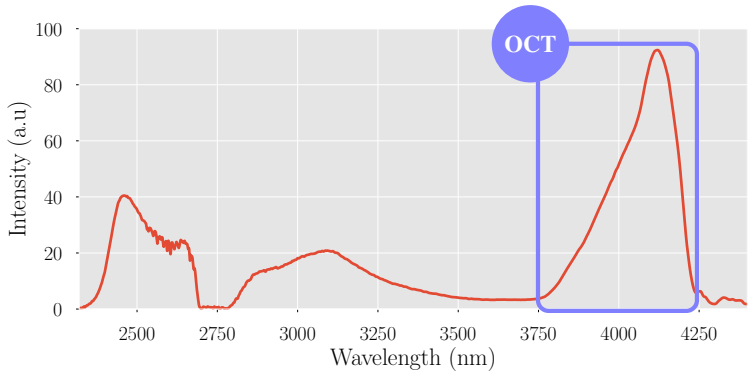

Fig. 1. Spectrum of the supercontinuum source measured by an FTIR spectrometer using a HgCdTe detector sensitive from 2 µm to 14 µm. A neutral density (ND) filter with an optical density (OD) of 1 is used to avoid the oversaturation. The spectral range being exploited for OCT measurements is indicated.

The broadband supercontinuum radiation is generated in a highly non-linear ZBLAN (ZrF_4-BaF_2-LaF_3-AlF_3-NaF) fiber leading to a maximum intensity located at 4.12 µm (long wavelength soliton). The spectral range between 3.75 µm and 4.25 µm was specified for OCT measurements due to the central wavelength (λ_c = 4 µm) of our interest, spectral shape and high average power (around 40 mW). Therefore, a set of longpass and bandpass spectral filters is used to select the range and avoid damage of the sample by light at other wavelengths.

2.2. Optical setup

The challenges for the MIR FD-OCT system are two-fold, namely the broad spectral range and the high costs and unavailability of devices for this wavelength region. Therefore, suitable optical components have to be chosen considering the trade-off between the performance and feasibility.

Optics EXPRESS

The developed OCT system (Fig. 2) is based on a free-space Michelson interferometer formed by a CaF_2 beam splitter (BS) and gold mirrors. In the sample arm of the system, an achromatic doublet (Thorlabs AC254-050-E, Si-Ge, focal length $F = 50$ mm) is used to focus light onto the object. Due to the corrected chromatism, the focal spot shift is minimized (less than 1 µm within the OCT range). The use of off-axis parabolic mirrors instead results in a degraded interference fringe visibility because of the double-pass-induced aberrations [21]; common singlets (CaF_2 or BaF_2) result in a focal spot shift up to several millimeters. Using the model of the doublet and initial beam parameters, a diffraction limited lateral resolution of 19.2 µm is obtained through the simulations of Gaussian beam propagation. The beam confocal parameter or the depth of focus is calculated to be around 1.1 mm for $\lambda = 4$ µm.

The lateral scanning of the sample is performed by a high precision stage (Physik Instrumente (PI) GmbH, 100 nm minimum step size) synchronized with the detection system.

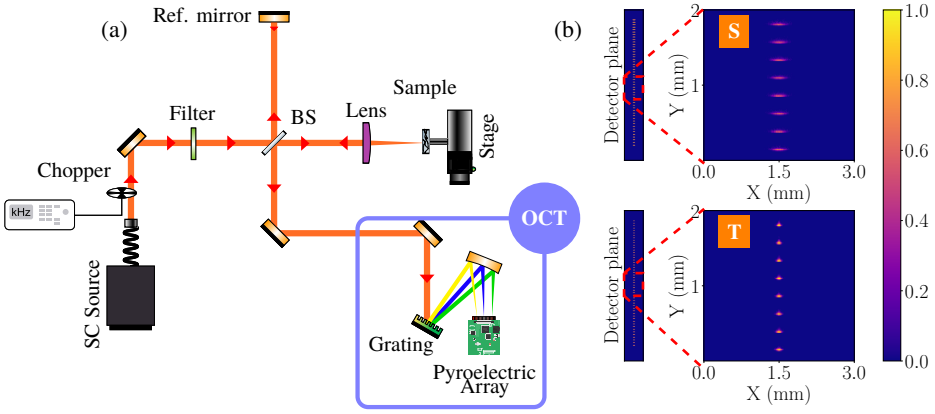

Fig. 2. (a) Schema of the MIR FD-OCT setup, (b) Simulated intensity distribution (logarithmic scale, normalized) in the array plane (X,Y coordinates) for the spectrum at discrete wavelengths, T - toroidal and S - spherical mirror.

To record the spectral interferogram, a low-cost $LiTaO_3$ pyroelectric focal linear array (DIAS Infrared GmbH) with 510 sensitive elements and pixel size of 20×500 µm^2 (a thickness of pyroelectric material 5-8 µm) is utilized as the detector. The array is integrated into a specially designed Czerny-Turner spectrometer formed by a blazed reflective grating (300 grooves/mm) and a spherical mirror with 100 mm focal length. For optimization, the setup has been simulated by ZEMAX. The toroidal mirror shows the best solution with reduced aberrations [Fig. 2 (b)], whereas a spherical mirror would offer a good compromise between the magnitudes of aberrations and financial costs. Due to the rectangular shape of the pixels, the influence of astigmatism caused by the spherical mirror is of minor effect. The spectral resolution of the spectrometer (around 3 nm) limits the theoretical imaging probing depth of FD-OCT to about 1.3 mm defined by the Nyquist theorem [22, 23]. The effective probing depth is actually limited by the depth of focus of the beam (1.1 mm), due to the optical design.

The schema of the setup depicted in Fig. 2 is not to scale. The interferometer is balanced by an additional free-space interval in the reference arm, while the doublet is corrected for chromatism. In this way, potential dispersion is reduced so that the degradation of axial resolution in OCT image is not observed.

2.3. *Pyroelectric linear array*

The spectral response of the $LiTaO_3$ detectors is relatively flat with a responsivity of 68×10^4 V/W in the mid-infrared wavelength range [16, 24]. However, the sensitive area was protected by a

Optics EXPRESS

0.5 mm thick silicon window (transparent for 2 µm - 6 µm) to avoid microphonic noise (specific to such detectors [25]) and reduce malfunction. The latter is caused by a photoelectric effect occurs for wavelengths below 1.5 µm in diodes and transistors in the electronics. The signal read-out scheme is presented by two CMOS circuits, i.e. 2×255 sensitive elements, alternating. A pitch of 25 µm is used for 20×500 µm^2 size of the pixels to reduce cross-talk.

The physical principle of pyroelectric detectors requires a light intensity modulation [26] that is implemented by a chopper synchronized with the evaluation board. The maximum spectral acquisition rate (i.e. OCT A-scan imaging) of 100 Hz is limited by the read-out electronics.

The detector noise equivalent power (NEP) is 1.2 nW as measured by the manufacturer with the 16-bit station (128 Hz light modulation frequency). The NEP value is documented in the test protocol and corresponds to a noise voltage of 1.3 mV. Practically, the low-cost 12-bit analog-to-digital converter (ADC), used in the experimental setup, sets the minimum step of the digitalization. Therefore, the root-mean-square voltage noise of 2.52 mV was measured under normal conditions, which limits the maximum achievable voltage (direct measurement) dynamic range. Increased noise is additionally introduced by the design of the detector evaluation board with two alternating application-specific integrated circuits, so that the measured signal shows slightly different values at the neighboring pixels.

The focal array can operate in a wide temperature range (-15°to 70°) and does not require additional cooling, since the pyroelectric effect is caused by the radiation changes [16, 26]. Therefore the measurements have been done after a warm-up time when the temperature of the array, measured by the internal detector, is stable.

2.4. *Post-processing and image artifacts*

The post-processing algorithm (as shown in Fig. 3) was applied to the particular configuration of the system presented in Fig. 2 in order to reduce the so-called ghost images and improve the signal-to-noise ratio (SNR).

The detector related noise is mainly caused by the non-linear behavior of the pixel-to-pixel beating in the registered signal [see Fig. 3(b), 1]. The difference introduces not only high frequency (Nyquist frequency, f_n) components in the final post-processed image, but also artifacts at lower frequencies arise due to the aliasing. Therefore, the first post-processing step involves a linear filtering of the frequencies higher than $0.95 f_n$ applied to the raw signal, while an additional averaging and chopper trigger delay are used to reduce the effects of time beating.

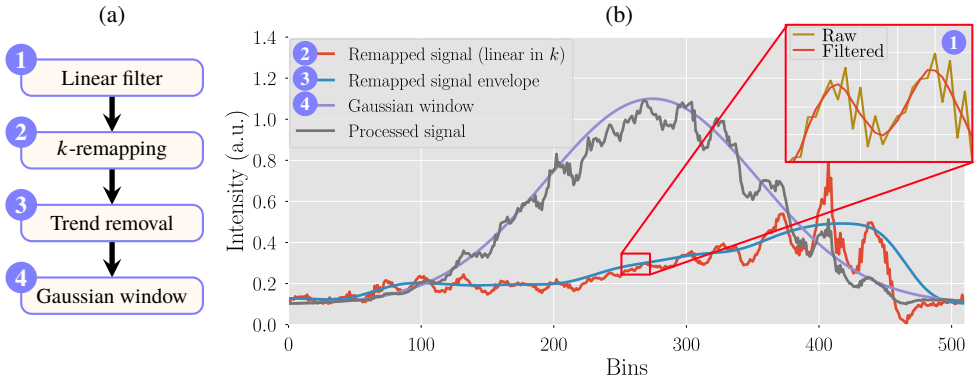

Fig. 3. (a) The post-processing algorithm flowchart, (b) Post-processing of the measured data where the processing steps are applied to the signal in k-space, ($k = 1/\lambda$); The zoomed-in detail represents the linear filtering step.

The filtered signal, from which the reference spectrum profile has been subtracted, is

Optics EXPRESS

equidistantly remapped into k-space by linear interpolation. The interference-free reference spectrum is obtained by blocking the sample arm. To reduce the effects caused by the sharp edge of the spectral peak (as shown in Fig. 1), an additional subtraction of the residual amplitude envelope (trend obtained through a Hilbert transform) is implemented. Finally, a discrete Fourier transform (DFT) is applied to the signal that is multiplied by a Gaussian window in the frequency domain. The width and position of the window are optimized to get a higher SNR for the lowest FWHM of an axial response function. The absolute value of DFT yields the structural intensity information over depth. Figure 3(b) demonstrates all the steps applied to the signal.

The residual artifacts, which can not be removed numerically, arise from the optical part, namely, from the second reflection from the plate beam splitter. Thereby, for relatively high reflective surfaces, ghost images at deeper layers might occur. For example, for the mirror surface near the zero delay plane and in the absence of any neutral density filters, the image artifacts can be observed outside the real probing depth limit; but for thicker structures with a defined refractive index it could appear between the real surfaces. Shifting the zero delay plane can distinguish the real layers, or, an additional diffusive cover can reduce this effect as well as auto-correlation components caused by the interference between the neighboring layers.

2.5. Sensitivity and resolution of the system

The sensitivity and the lateral and axial resolutions of the system are evaluated (see Fig. 4). The former is traditionally defined as the maximum $\mathrm{SNR}_{\max}$ [12] which was obtained using a gold mirror with a reflectivity $R_{\mathrm{m}} = 0.98$ positioned at about 0.1 mm from the zero delay plane. To avoid the oversaturation of the detector, an ND filter (OD = 1) was used in the sample arm. Then the sensitivity is calculated as [27]:

$$\mathrm{SNR}_{\max} = 20 \log \frac{I_{\mathrm{m}}}{\sigma} - 10 \log(R_{\mathrm{m}} \cdot T^2), \tag{1}$$

where I_{m} is the peak intensity value at the mirror surface of the b-scan, σ is the standard deviation of ambient noise floor calculated for the same OCT image [28], see Fig. 4(a); T is the transmittance of the filter (T^2 represents the double pass). The factor of 20 (or square in the traditional definition) arises since I_{m} is proportional to the amplitude of interference fringes, but not to the optical power.

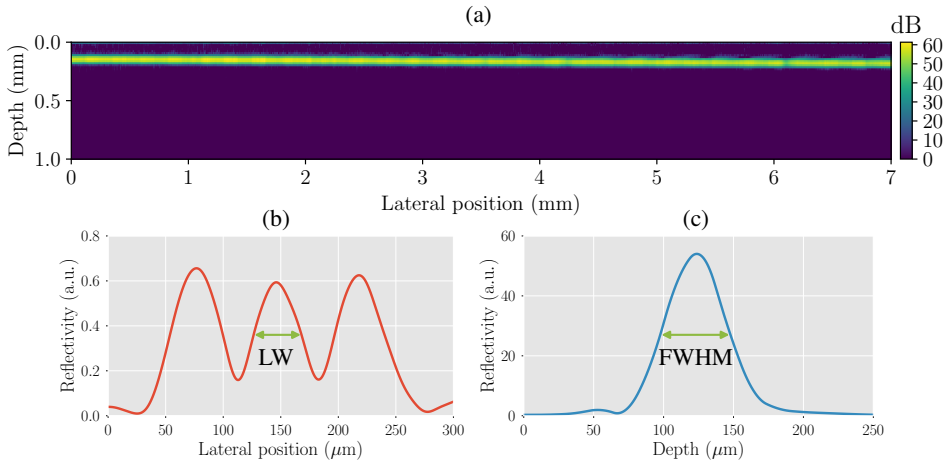

Fig. 4. (a) B-scan of the gold mirror with ND filter in the sample arm (OD = 1), (b) Lateral resolution measured using a USAF resolution test target, the line width (LW) is 35.08 μm, (c) Axial response function defined for mirror surface (about 50 μm FWHM).

Optics EXPRESS

According to Eq. (1), it yields a sensitivity of 81.7 dB measured at a light modulation frequency of 100 Hz (maximum limited by the read-out electronics).

The lateral resolution of the system was determined using a 1951 USAF resolution test target in two configurations: with and without a 0.3 mm alumina (Al_2O_3) wafer on top. In the case of the first test structure, the smallest line width which can be resolved by the system is around 56 µm. Without the alumina cover plate, the lateral resolution, i.e. minimum resolvable distance, of approximately 35 µm was achieved. Figure 4(b) shows a lateral cross-section for the element number 6, the 3rd group. The disagreement with the theoretical resolution (19.2 µm) could originate from the wide spectral output and the different monochromatic beam sizes of the supercontinuum after the collimation and the focusing optics [29].

In order to define the axial resolution, a depth calibrated OCT A-scan for a highly reflective surface (gold mirror) was obtained. Figure 4(c) depicts the corresponding axial point spread function with FWHM around 50 µm in air, which agrees with the theoretical value around 45 µm defined by the coherence length [30–32], determined by the selected part of the spectrum (150 nm FWHM).

2.6. Samples

2.6.1. Ceramic plates

Ceramic samples are of particular interest for applications in NDT. Two ceramic plates, a single-crystal sapphire wafer and a polished zirconia (ZrO_2) plate, were prepared as specimens. The sapphire wafer has a relatively rough top surface and a polished rear surface. The zirconia sample has a porosity around 0.2% and a mean air pore diameter of 0.2 µm; it was covered by a highly diffusive tape to reduce the strong surface reflection (similar to a refractive index matching gel).

2.6.2. Complex ceramic sample

A multilayer alumina (Al_2O_3) sample similar to the one simulated in [7] was assembled together [see Fig. 5(a)]. The structure is formed by two sintered plates: the top 0.3 mm thick continuous layer is covered by a diffusive tape and placed at around 0.1 mm above the second sintered alumina layer with a thickness of 0.45 mm. In the top surface of the second layer, there is a series of laser milled microchannels with variable widths (starting from approximately 150 µm) and height of approximately 65 µm. The porosity of both plates is approximately 1% and characterized by a mean air pore diameter of 0.4 µm.

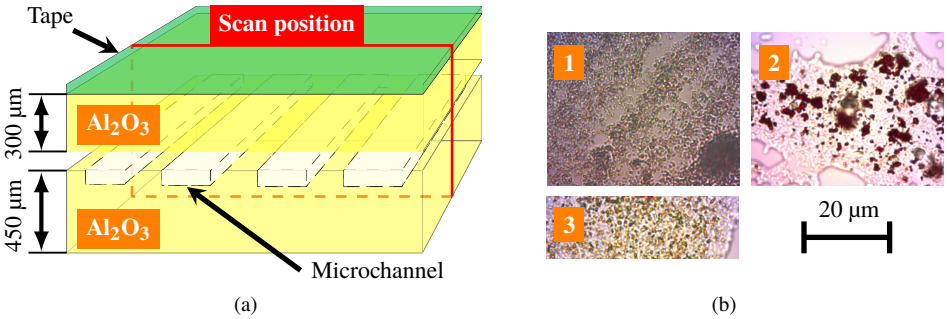

Fig. 5. Illustration of the specimens: (a) Schematic model of the multilayer ceramic sample, (b) Bright field microscopy images of color pigments in thin paint layer samples: 1 - white titanium, 2 - cadmium red, 3 - yellowish green.

2.6.3. Oil paint test samples

Oil and other paint layers create specimens that are highly scattering and absorbing in NIR or VIS spectral ranges. For testing our OCT system, we prepared a linseed oil paint test sample which

Optics EXPRESS

was mainly made up with 3 different colors (partly mixed with each other and inhomogeneous): white titanium (titanium dioxide pigment), cadmium red (PR108 pigment) and yellowish green (mixture of PG7 and PY74 pigments). The pigment code names can be used to define the chemical composition of each paint, e.g. PG7 is cu-poly-chlorophthalocyanine [33]. The paints were applied to the substrate and covered by a varnish layer. The mean thickness of the sample was about 0.5 mm.

The microscope images of thin paint layers are shown in Fig. 5(b). The sizes of the pigment components that strongly influence light scattering [34] are quite similar for the titanium white and yellowish green paints (mean around 1 µm), while the cadmium red constituents demonstrate a tendency to merge in clusters with a mean diameter size around 5 µm.

3. Results

3.1. Proof of concept

The MIR FD-OCT cross-sectional scans (B-scans) and A-scans (extracted at center of the B-scans and normalized by maximum magnitude) of the simple ceramic plate structures (see Fig. 6) were measured in order to prove the feasibility of the concept. To verify the results and compare the performance, the images of the same samples were also obtained with a commercial NIR FD-OCT system (Thorlabs Vega, λ_c = 1.3 µm).

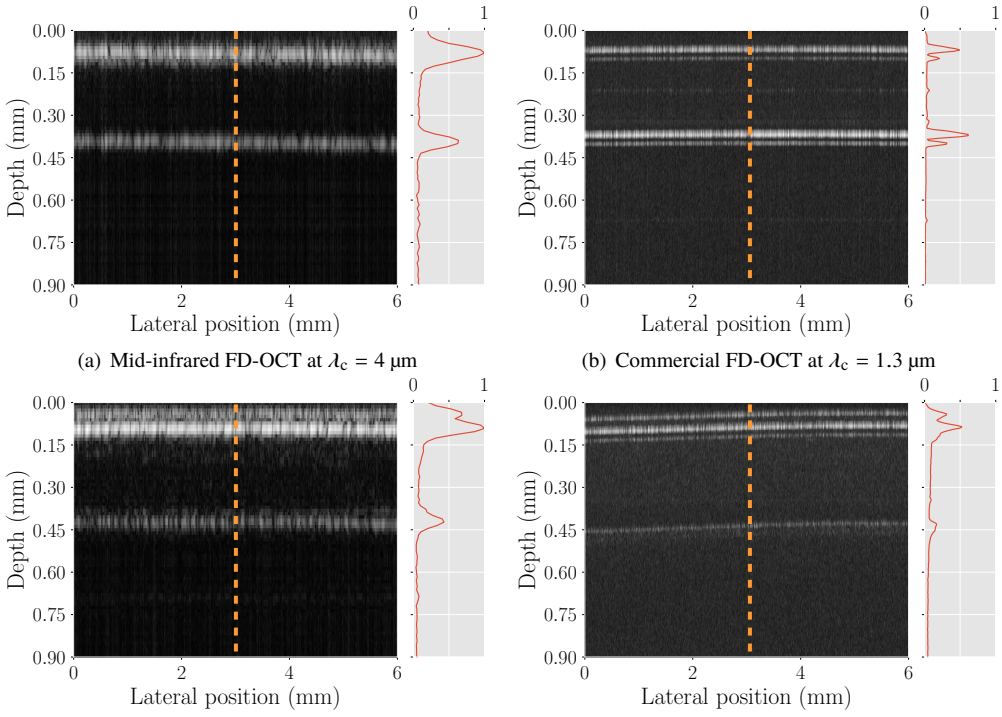

(a) Mid-infrared FD-OCT at λ_c = 4 µm

(b) Commercial FD-OCT at λ_c = 1.3 µm

(c) Mid-infrared FD-OCT at λ_c = 4 µm

(d) Commercial FD-OCT at λ_c = 1.3 µm

Fig. 6. B-scans and A-scans (at dashed lines) of the single-crystal sapphire wafer (a,b) with the rough surface facing upwards (300 µm thickness) and of (c,d) the zirconia plate (300 µm thickness) covered by a diffusive tape.

The systems operate in different spectral regions. For the MIR FD-OCT system, a higher penetration depth for strongly scattering samples can be expected. In order to achieve an axial resolution comparable to that of the NIR OCT system, the spectral bandwidth of the MIR system

Optics EXPRESS

needs to be significantly extended, which then introduces technical problems in spectrometer design. Additionally, for the extended bandwidth, the sensitivity decay is stronger due to the finite resolution of the spectrometer and reduced fringe visibility at higher frequencies [23, 35]. Therefore, the MIR FD-OCT system is optimized with respect to the trade-off between resolution and sensitivity roll-off.

Both systems demonstrate a similar penetration depth and visibility of the top and rear surfaces for the single-crystal sapphire wafer because there is no bulk scattering. However, the A-scans show a lower signal level for the rough top surface recorded by the 1.3 µm FD-OCT system due to the higher surface scattering. In contrast, scattering by the rough surface is much weaker in the MIR system [36].

The enhanced performance becomes noticeable for the measurements of the zirconia plate which has a higher scattering coefficient for shorter wavelengths [7], while the OCT image and corresponding A-scans obtained at the MIR wavelengths show a pronounced intensity peak corresponding to the rear surface.

3.2. Multilayer ceramic sample

The cross-sectional scans of the complex ceramic sample described above are presented in Fig. 7. The refractive index of alumina ($n = 1.675$ for $\lambda = 4$ µm and $n = 1.75$ for $\lambda = 1.3$ µm [37]) was taken into account during the measurements to define the correct depth range.

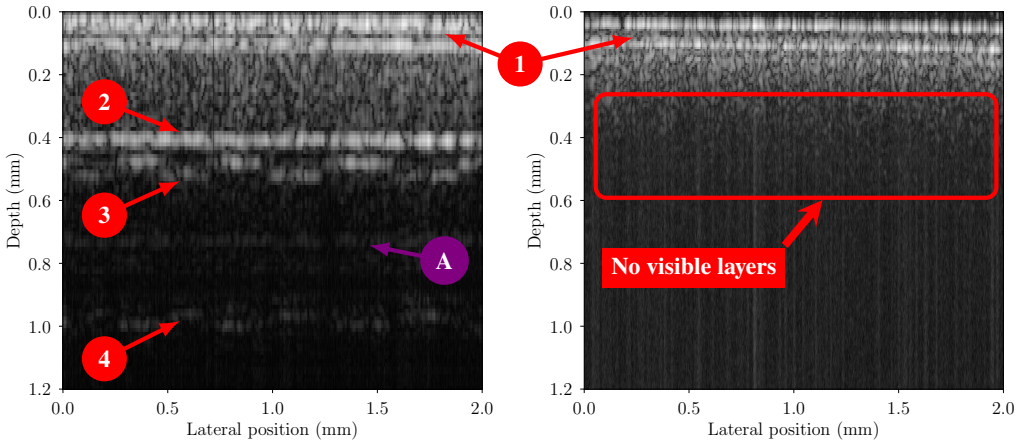

(a) Mid-infrared FD-OCT at $\lambda_c = 4$ µm (b) Commercial FD-OCT at $\lambda_c = 1.3$ µm

Fig. 7. Comparison measurements of the multilayer ceramic structure: 1 and 2 - surfaces of the 300 µm thick alumina plate (top surface covered by a diffusive tape); 3 - first surface of 450 µm alumina plate with micro-channels and 4 - rear surface of this plate. A - image artifact caused by the interference of the second surface and the beam-splitter.

The effective penetration depth of the 1.3 µm FD-OCT system is mainly limited by the strong bulk scattering caused by the pores in ceramics which are in the size scale of the wavelength range. As demonstrated in [7] the scattering coefficient (that can be obtained through the Mie theory) at NIR wavelengths is much higher than that for the MIR region. Therefore, only the top surface of the sample was observed [see Fig. 7(b)], while the MIR FD-OCT system demonstrates a significantly enhanced effective penetration depth by successfully detecting all the four surfaces (marked as 1-4 in Fig. 7), which is the major advantage of the MIR system.

The reflectivity gradients, layer visibility and boundary contrast of the B-scans obtained by both systems agree very well with the theoretical prediction in [7] as well as the effect that the image of the rear surface of the second plate (Fig. 7, surface 4) is distorted by the optical path

Optics EXPRESS

difference.

The visibility of the layers can be increased by removing of the diffusive cover, but it will introduce several ghost surfaces (similar to "A" in Fig. 7(a) presenting an unreal surfaces inside the material) because of the stronger interference between the surfaces and the beam splitter; alternatively the sample can be slightly tilted for reducing the specular reflection.

3.3. Oil paint test samples

We examined the system performance for oil paint layers (see Fig. 8) that are constantly of interest in art diagnosis. They are difficult to investigate using traditional OCT operating in VIS and NIR regions due to the strong scattering and absorption by constituent pigments. Enhanced penetration depth has already been reported for a 2 µm FD-OCT system [15]. Nevertheless, the investigation of thick layers of Titanium dioxide (white titanium paint) with OCT remains an issue [38, 39]. Here, we show the enhanced detection and imaging capability by using the MIR FD-OCT system and its potential applications in this field.

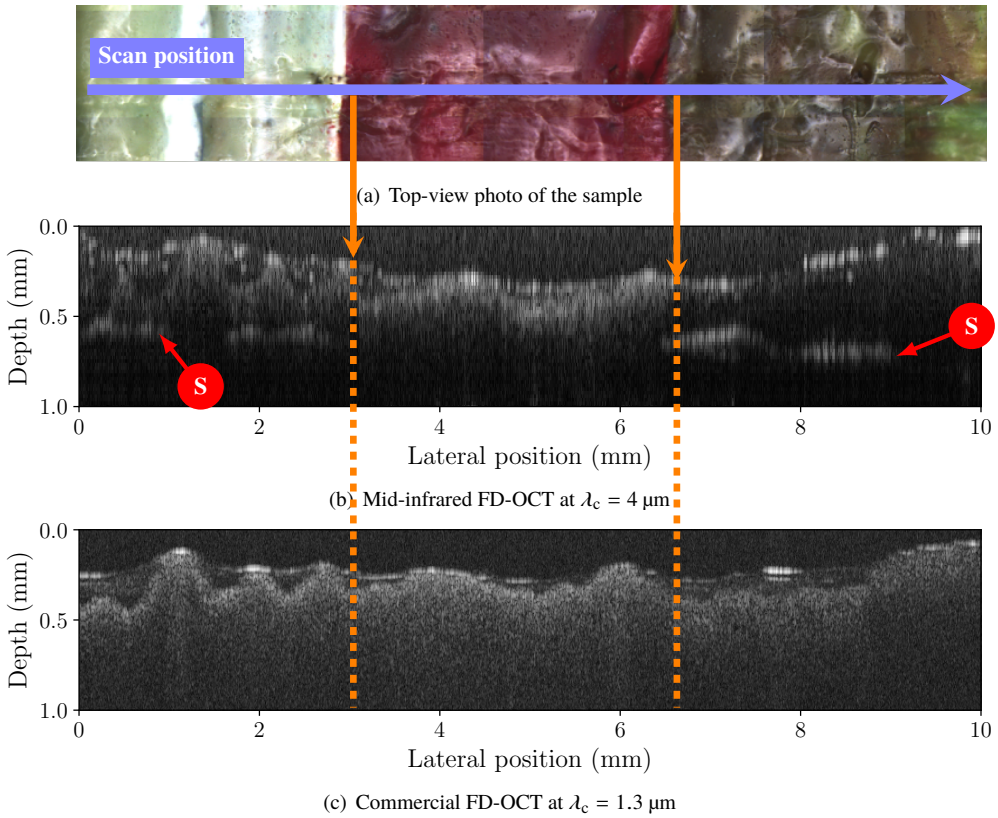

Fig. 8. Comparison measurements (b,c) of a lacquered oil paint test sample (a) on the substrate made up by white titanium, cadmium red and yellowish green correspondingly (S - substrate surface)

The cross-sectional MIR FD-OCT images appeared more detailed and complex: in the case of white titanium and yellowish green paints, the substrate (marked as S) is revealed, which is located at a depth of 0.5 mm below the top surface. The paints can be easily distinguished since the magnitudes of bulk scattering are different. For example, the OCT signal in the region of the red paint with relatively big cadmium-based pigments is attenuated more rapidly compared to

Optics EXPRESS

the white and green paints. In contrast, multiple scattering is dominant for the 1.3 µm system, so that the image cannot differentiate the types of paints, the subsurfaces are not visible.

4. Conclusion and Outlook

In this contribution, we have introduced a mid-infrared (MIR) Fourier-domain optical coherence tomography (FD-OCT) that operates in the wavelength region around 4 µm, works in a spectral domain configuration (imaging speed around 2.5 A-scans/s), and is equipped with the pyroelectric line detector. The MIR FD-OCT system is developed and optimized for aberrations, image artifacts, detector noise, as well as shows a moderate price. The system has been experimentally characterized: the axial resolution of 50 µm, lateral resolution of 35 µm and the sensitivity of 81.7 dB have been demonstrated. Thereby, we achieved a 22 dB advantage in sensitivity compared to a MIR time-domain system reported in [9].

Experimental evidence of the significantly enhanced penetration depth into materials have been shown by comparing the imaging results of the system we developed with a state-of-the-art commercial 1.3 µm FD-OCT for the alumina ceramics and the oil paint samples. However, it should be mentioned, that the OCT spectral window must be chosen suitable for the specific application, i.e. the imaging depth of MIR OCT system could also degrade for samples with a high water content due to the strong absorption in this wavelength range.

This MIR FD-OCT system is novel, to the best of our knowledge, opens up many new application fields for OCT-based NDT, e.g. quality inspection of ceramics, art diagnosis, polymers etc. Regarding the price of the system, this is an elegant low-cost solution using pyroelectric detectors. The supercontinuum sources in MIR are still expensive, but it is expected that their prices will decrease in the near future because of the high demand. Furthermore, other novel light sources in the MIR range are emerging or under development [40].

This MIR FD-OCT system could still be improved by adaptation of read-out electronics of the pyroelectric array for OCT applications, e.g. using the higher harmonics of the light modulation shows a better fringe visibility, but on the other hand it may increase the beating and drift of the signal. Meanwhile, an optimized optical setup, e.g. using a cube beam splitter instead of a plate, could enhance the image quality and remove double interference artifacts noticeable for highly reflective samples.

Considering the potential offered by the supercontinuum sources in the mid-infrared spectral range [41], we are expecting an effective combination of two NDT techniques in the near future: MIR FD-OCT and vibrational spectroscopy [42]. Certainly, spectroscopic MIR OCT should be the main goal in order to get depth resolved spectra, but there still remains a technical problem due to the limited resolution of the spectrometers in this wavelength range. As another option, a spectroscopy modality, e.g. based on a Fabry-Pérot tunable filter, can be integrated into the MIR FD-OCT setup in order to supplement the structural information with spatially resolved reflectance spectra (e.g. co-registered in the extended spectral range). This will offer new options for the development of multimodal imaging and envisage novel use-cases for e.g. pharmaceutical applications.

Funding

Horizon 2020 Framework Programme (722380); Province of Upper Austria (Innovative Upper Austria 2020); EFRE Urban Innovative Actions (IWB2020).

References

1. J. Kilgus, K. Duswald, G. Langer, and M. Brandstetter, "Mid-infrared standoff spectroscopy using a supercontinuum laser with compact fabry-pérot filter spectrometers," Appl. Spectrosc. **72**, 634–642 (2018). PMID: 29164925.
2. D. Stifter, "Beyond biomedicine: a review of alternative applications and developments for optical coherence tomography," Appl. Phys. B **88**, 337–357 (2007).

Optics EXPRESS

3. J. Golde, L. Kirsten, C. Schnabel, J. Walther, and E. Koch, *Optical Coherence Tomography for NDE* (Springer International Publishing, Cham, 2018), pp. 1–44.
4. J. Jang, J. Lim, H. Yu, H. Choi, J. Ha, J.-H. Park, W.-Y. Oh, W. Jang, S. Lee, and Y. Park, "Complex wavefront shaping for optimal depth-selective focusing in optical coherence tomography," Opt. Express **21**, 2890–2902 (2013).
5. S. Liu, M. R. E. Lamont, J. A. Mulligan, and S. G. Adie, "Aberration-diverse optical coherence tomography for suppression of multiple scattering and speckle," Biomed. Opt. Express **9**, 4919–4935 (2018).
6. S. Popoff, G. Lerosey, M. Fink, A. C. Boccara, and S. Gigan, "Image transmission through an opaque material," Nat. Commun. **1**, 81 (2010).
7. R. Su, M. Kirillin, E. W. Chang, E. Sergeeva, S. H. Yun, and L. Mattsson, "Perspectives of mid-infrared optical coherence tomography for inspection and micrometrology of industrial ceramics," Opt. Express **22**, 15804–15819 (2014).
8. D. Huang, E. A. Swanson, C. P. Lin, J. S. Schuman, W. G. Stinson, W. Chang, M. R. Hee, T. Flotte, K. Gregory, G. A. Puliafito, and J. G. Fujimoto, "Optical coherence tomography," Science **254**, 1178–1181 (1991).
9. C. S. Colley, J. C. Hebden, D. T. Delpy, A. D. Cambrey, R. A. Brown, E. A. Zibik, W. H. Ng, L. R. Wilson, and J. W. Cockburn, "Mid-infrared optical coherence tomography," Rev. Sci. Instruments **78**, 123108 (2007).
10. D. Varnell, M. C. Zheng, M. Chow, and C. Gmachl, "Spectroscopy and imaging using a mid-ir quantum cascade optical coherence tomography (oct) system," in *Conference on Lasers and Electro-Optics,* (Optical Society of America, 2016), p. ATu1J.7.
11. A. V. Paterova, H. Yang, C. An, D. A. Kalashnikov, and L. A. Krivitsky, "Tunable optical coherence tomography in the infrared range using visible photons," Quantum Sci. Technol. **3**, 025008 (2018).
12. R. Leitgeb, C. K. Hitzenberger, and A. F. Fercher, "Performance of fourier domain vs. time domain optical coherence tomography," Opt. Express **11**, 889–894 (2003).
13. N. Nassif, B. Cense, B. H. Park, S. H. Yun, T. C. Chen, B. E. Bouma, G. J. Tearney, and J. F. de Boer, "In vivo human retinal imaging by ultrahigh-speed spectral domain optical coherence tomography," Opt. Lett. **29**, 480–482 (2004).
14. M. A. Choma, M. V. Sarunic, C. Yang, and J. A. Izatt, "Sensitivity advantage of swept source and fourier domain optical coherence tomography," Opt. Express **11**, 2183–2189 (2003).
15. C. S. Cheung, J. M. O. Daniel, M. Tokurakawa, W. A. Clarkson, and H. Liang, "High resolution fourier domain optical coherence tomography in the 2 μm wavelength range using a broadband supercontinuum source," Opt. Express **23**, 1992–2001 (2015).
16. A. Rogalski, *Infrared Detectors 2nd Edition* (CRC, 2011).
17. S. Wolf, J. Kiessling, M. Kunz, G. Popko, K. Buse, and F. Kühnemann, "Upconversion-enabled array spectrometer for the mid-infrared, featuring kilohertz spectra acquisition rates," Opt. Express **25**, 14504–14515 (2017).
18. J. S. Dam, K. P. Sørensen, C. Pedersen, and P. Tidemand-Lichtenberg, "Mid-ir image acquisition using a standard ccd camera," in *Frontiers in Optics 2010/Laser Science XXVI,* (Optical Society of America, 2010), p. FWX5.
19. A. Barh, C. Pedersen, and P. Tidemand-Lichtenberg, "Ultra-broadband mid-wave-ir upconversion detection," Opt. Lett. **42**, 1504–1507 (2017).
20. A. Barh, P. Tidemand-Lichtenberg, and C. Pedersen, "Thermal noise in mid-infrared broadband upconversion detectors," Opt. Express **26**, 3249–3259 (2018).
21. J. E. Howard, "Imaging properties of off-axis parabolic mirrors," Appl. Opt. **18**, 2714–2722 (1979).
22. A. F. Fercher, "Optical coherence tomography," J. Biomed. Opt. **1**, 1 – 17 (1996).
23. S. W. Lee, H. W. Jeong, B. M. Kim, Y. C. Ahn, W. Jung, and Z. Chen, "Optimization for axial resolution, depth range, and sensitivity of spectral domain optical coherence tomography at 1.3 um," J. Korean Phy. Soc. **55**, 2354–2360 (2009).
24. J. Lehman, "Pyroelectric trap detector for spectral responsivity measurements," Appl. Opt. **36**, 9117–9118 (1997).
25. H. Budzier and G. Gerlach, *Thermal Infrared Sensors: Theory, Optimisation and Practice* (John Wiley & Sons, 2011).
26. A. Hossain and M. H. Rashid, "Pyroelectric detectors and their applications," IEEE Transactions on Ind. Appl. **27**, 824–829 (1991).
27. A. Agrawal, T. J. Pfefer, P. D. Woolliams, P. H. Tomlins, and G. Nehmetallah, "Methods to assess sensitivity of optical coherence tomography systems," Biomed. Opt. Express **8**, 902–917 (2017).
28. D. J. Fechtig, T. Schmoll, B. Grajciar, W. Drexler, and R. A. Leitgeb, "Line-field parallel swept source interferometric imaging at up to 1 mhz," Opt. Lett. **39**, 5333–5336 (2014).
29. I. J. Arnold, H. Moosmüller, N. Sharma, and C. Mazzoleni, "Beam characteristics of fiber-based supercontinuum light sources with mirror- and lens-based beam collimators," Opt. Express **22**, 13860–13869 (2014).
30. A. F. Fercher, "Optical coherence tomography," J. Biomed. Opt. **1**, 1 – 1 – 17 (1996).
31. W. Drexler and J. G. Fujimoto, *Optical Coherence Tomography, Technology and Applications* (Springer International Publishing, 2008).
32. A. F. Fercher, W. Drexler, C. K. Hitzenberger, and T. Lasser, "Optical coherence tomography - principles and applications," Reports on Prog. Phys. **66**, 239–303 (2003).
33. G. Poldi and S. Caglio, "Phthalocyanine identification in paintings by reflectance spectroscopy. a laboratory and in situ study," Opt. Spectrosc. **114**, 929–935 (2013).
34. H. Liang, K. Keita, B. Peric, and T. Vajzovic, "Pigment identification with optical coherence tomography and multispectral imaging," in *Proc. OSAV 2008, the 2nd International Topical Meeting on Optical Sensing and Artificial*

Optics EXPRESS

Vision, (2008).
35. S. H. Yun, G. J. Tearney, B. E. Bouma, B. H. Park, and J. F. de Boer, "High-speed spectral-domain optical coherence tomography at 1.3 μm wavelength," Opt. Express **11**, 3598–3604 (2003).
36. J. M. Bennett and L. Mattsson, *Introduction to Surface Roughness and Scattering* (Optical Society of America, 1999).
37. I. H. Malitson, "Refraction and dispersion of synthetic sapphire," J. Opt. Soc. Am. **52**, 1377–1379 (1962).
38. C. S. Cheung, M. Tokurakawa, J. M. O. Daniel, W. A. Clarkson, and H. Liang, "Long wavelength optical coherence tomography for painted objects," in *Optics for Arts, Proc.SPIE,* vol. 8790 (2013), pp. 1–5.
39. H. Liang, C. S. Cheung, J. M. O. Daniel, M. Tokurakawa, W. A. Clarkson, and M. Spring, "High resolution fourier domain optical coherence tomography at 2 microns for painted objects," in *Proc.SPIE,* vol. 9527 (2015), pp. 9527 – 9527 – 6.
40. C. C. Hou, H. M. Chen, J. C. Zhang, N. Zhuo, Y. Q. Huang, R. A. Hogg, T. D. Childs, J. Q. Ning, Z. G. Wang, F. Q. Liu, and Z. Y. Zhang, "Near-infrared and mid-infrared semiconductor broadband light emitters," Light. Sci. Appl. **7**, 17170 (2018).
41. J. Kilgus, G. Langer, K. Duswald, R. Zimmerleiter, I. Zorin, T. Berer, and M. Brandstetter, "Diffraction limited mid-infrared reflectance microspectroscopy with a supercontinuum laser," Opt. Express **26**, 30644–30654 (2018).
42. D. C. Harris and M. D. Bertolucci, *Symmetry and Spectroscopy : Introduction to Vibrational and Electronic Spectroscopy* (Dover Publications Inc., 1989).